Nucleation and Wake-chopping in Low Pressure Steam Turbines

Journal Title
XX(X):1–11

DOI: 10.1177/ToBeAssigned
www.sagepub.com/
SAGE

Fiona R. Hughes[1], Jörg Starzmann[1], and Alexander J. White[1]

Abstract

While wetness formation in steady flows such as nozzles and cascades is well-understood, predicting the polydispersed droplet spectra observed in turbines remains challenging. The characteristics of wetness formation are affected by the expansion rate at the Wilson point. Because the expansion rate varies substantially both axially and circumferentially within steam turbines, the location of the Wilson point within a blade row is a primary factor determining the droplet spectrum and phase change losses. This effect is first investigated using a single streamline with a varying expansion rate, and it is shown that the phase change losses during spontaneous condensation are highest when a large region of high subcooling precedes the Wilson point. The conditions resulting in the highest wetness loss in the nucleation zone do not correspond to those that produce the largest downstream droplets.

The effect of nucleation location is then assessed using a non-equilibrium RANS calculation of a realistic low pressure (LP) steam turbine geometry. A quasi-three dimensional (Q3D) flow domain is used to simplify the analysis, which is performed both steadily and unsteadily to isolate the effects of wake-chopping. The inlet temperature is varied to investigate the impact of the Wilson point location on the steady and unsteady wetness loss and droplet spectra. The trends observed in the 1D analysis are repeated in the steady RANS results. The unsteady results show that the Wilson zone is most sensitive to wake-chopping when located near a blade trailing edge and the following inter-row gap. The predicted wetness losses are compared to those predicted by the Baumann rule.

Keywords

Low pressure steam turbines, condensation, wetness loss, unsteady effects

Introduction

From condensing flow experiments in nozzles[1], it is known that the conditions at the Wilson point, defined as the location of maximum subcooling, determine the resulting downstream wetness properties. These include the droplet spectrum and the loss generated by irreversible heat transfer. This relationship is straightforward in nozzles where the flow expands near-monotonically. Higher expansion rates lead to higher subcooling at the Wilson point, higher peak nucleation rates, and smaller droplets[2,3]. Although there are still uncertainties in the modelling process[4], downstream nozzle conditions can be estimated with satisfactory accuracy[5,6].

The connection between the expansion rate at the Wilson point and the downstream droplet spectra holds true in steam turbines, but the more complicated flow field makes the properties at the Wilson point dependent on its precise physical location and therefore more challenging to predict. Experimental studies in cascades[7] have shown that wetness is affected by the local expansion rate and its cross-passage variation, as well as by the presence of shock waves. However, because nucleation can only occur in the supersonic region in flows without work extraction, the Wilson zone always occurs downstream of the throat in cascade experiments. In steam turbines, nucleation may occur at subsonic flow speeds. RANS calculations have successfully predicted both the location of the Wilson zone in cascades and the interaction with the shock structure[7,8].

The phenomenon of wake-chopping has been used to explain the distinctive droplet spectra observed in steam turbines[9]. Wake-chopping occurs when wakes from a given blade row are intersected and divided by the blades in the following row. The fluid entrained in the boundary layers of preceding blade rows is warmer than that of the freestream flow and can impact nucleation and droplet growth as it is swept through downstream blade passages. The effect of wake-chopping on wetness formation has been investigated in a statistical sense[9,10], but it has not been clearly demonstrated using unsteady RANS simulations.

This paper seeks to analyse in detail the impact of those features that differentiate condensation in steam turbines from that in nozzles and cascades. First, the effect of a repeating axial variation in expansion rate is analysed in one dimension using a representative repeating pressure profile. Next, the two-phase, non-equilibrium RANS solver STEAMBLOCK and the quasi-three dimensional (Q3D) geometry are described. The Q3D flow domain eliminates tip leakage effects and hub and shroud vortices that would unnecessarily complicate the results. Steady and unsteady results for a range of inlet temperatures are

[1]Cambridge University Engineering Department, UK

Corresponding author:
Fiona R. Hughes, Whittle Laboratory, Cambridge University Engineering Department, 1 JJ Thomson Ave, Cambridge, Cambs CB3 0DY, UK.
Email: frh25@cam.ac.uk

presented, demonstrating the effect of the varying Wilson point location. Finally, the steady and unsteady flow fields are compared in detail to demonstrate the variations in irreversibility and droplet size caused by wake-chopping.

RANS Solver for Non-equilibrium Steam Flows

The RANS calculations presented below were performed using STEAMBLOCK, a non-equilibrium wet steam solver based on the three-dimensional viscous Euler solver TBLOCK[11]. STEAMBLOCK is an extension of the same method that includes two-phase non-equilibrium effects via the moment method[12].

The numerical scheme is the explicit "SCREE" scheme with spatially varied time steps[13]. For unsteady calculations, a dual time-stepping (DTS) method[14] is used. The Spalart-Allmaras one equation model is used to model turbulence[15]. A slip condition is applied at solid boundaries and the shear stresses are then computed from wall functions[16]. Within each time-step, adaptive smoothing is applied to ensure numerical stability[17]. A switching parameter is used to reduce fourth order smoothing and apply second order smoothing in regions of rapid variation in pressure and wetness fraction.

Modelling the Liquid Phase

The moment method was first applied to wet steam by Hill[18] and is described in detail by White and Hounslow[19]. Chandler et al.[12] describe the integration of the moment method with the TBLOCK RANS solver. In addition to the five equations needed to model flow in a single phase (continuity, momentum conservation, and energy conservation), four further equations are used to calculate the moments of the droplet spectrum. The numerical scheme conserves mixture properties which are calculated from the gas and liquid conditions. For example, mixture enthalpy h is:

$$h = (1-y)h_g(T_g, p) + yh_f(T_s, p), \tag{1}$$

in which y is the liquid mass fraction. The vapour enthalpy h_g and other vapour properties are evaluated at the local pressure p and vapour temperature T_g, while the liquid enthalpy h_f and other liquid properties are evaluated at the local pressure p and the local saturation temperature T_s. This neglects variations in liquid properties with droplet size that occur due to capillarity effects. These are only significant for very small droplets and therefore the resulting error is small. Steam properties are found using the look-up table method developed by Hill et al.[20] and the IAPWS Industrial Formulation (IF97)[21].

The classical nucleation rate[22] including a non-isothermal correction has been used for the results presented below. Therefore the nucleation rate J ($\mathrm{kg^{-1}s^{-1}}$) is given by

$$J = \frac{1}{1+\phi} q_c \frac{\rho_g^2}{\rho_f} \left(\frac{2\sigma}{\pi m^3}\right)^{1/2} exp\left(\frac{-4\pi r_*^2 \sigma}{3kT_g}\right). \tag{2}$$

in which ϕ is defined as[23]

$$\phi = \frac{2(\gamma-1)}{(\gamma+1)} \frac{h_{fg}}{RT_g} \left(\frac{h_{fg}}{RT_g} - \frac{1}{2}\right). \tag{3}$$

q_c is the condensation coefficient (assumed to equal 1.0), m is the mass of a single molecule, k is Boltzmann's constant, σ is the surface tension, and r_* is the Kelvin-Helmholtz critical radius.

The growth rate is that derived by Young[24]:

$$\frac{dr}{dt} = \frac{\lambda \Delta T (1 - \frac{r_*}{r})}{h_{fg}\rho_f r \left[1 + 3.78(1-\nu)\frac{Kn}{Pr}\right]}, \tag{4}$$

where λ is the vapour thermal conductivity, h_{fg} is the latent heat of vaporisation, and Kn and Pr are the Knudsen and Prandtl numbers, respectively. ΔT is subcooling, the difference between the local saturation temperature T_s and the gas temperature T_g. The capillarity term $(1 - \frac{r_*}{r})$ is included to accurately model the growth of droplets near to the critical size r_*. ν is a function recommended to account for the temperature difference between the current and equilibrium droplet sizes, and takes the form

$$\nu = \frac{RT_s}{h_{fg}} \left[\alpha - \frac{1}{2} - \frac{2-q_c}{2q_c}\left(\frac{\gamma-1}{\gamma}\right)\frac{c_pT_s}{h_{fg}}\right]. \tag{5}$$

R is the specific gas constant for steam and α is an empirical coefficient which is taken to equal 9.0 in the calculations presented. γ is the isentropic exponent and c_p is the vapour heat capacity at constant pressure.

Hughes et al.[25] compared the moment methods with Lagrangian full spectrum methods and demonstrated that it achieves satisfactory accuracy (errors in Sauter mean radius and entropy gain due to phase change $\leq$ 10%) for primary nucleation at the expansion rates present in LP steam turbines. Further details regarding the modelling methods can be found in Hughes[26].

Varying Axial Expansion Rate

Droplet nucleation and growth is first investigated within a single streamline containing an axially repeating pressure variation. This analysis is performed in the Lagrangian frame using the two-phase fluid particle solver described by Young[27]. Trajectories of pressure and viscous entropy generation versus time are supplied as inputs and the growth of the liquid phase is predicted, including the droplet spectrum and entropy generation due to phase change. The solver marches along the prescribed flow conditions using time increments chosen based on the local expansion rate, nucleation rate, and droplet relaxation time. A unique droplet group is formed within each nucleating time increment. The assumed pressure trajectory is similar to that seen in the passage centre and near the pressure side of a typical low pressure (LP) blade row and is repeated six times to be comparable to the repeating stage calculations presented below. The inlet temperature is varied from 436 K to 480 K, which corresponds to an inlet subcooling range between -22 K and -66 K.

Figure 1a shows the axial pressure variation and the Wilson point locations for each inlet temperature. The Wilson points are not evenly spaced, but instead are clustered in the high expansion rate region near each trailing edge. Figure 1b plots the peak subcooling at the Wilson points and the outlet Sauter mean radii against inlet temperature (bottom axis) and inlet subcooling (top axis). The peak subcooling

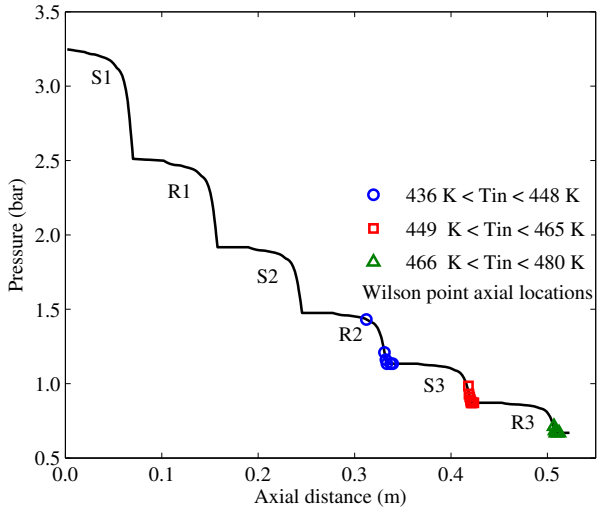

(a) Pressure and Wilson point locations

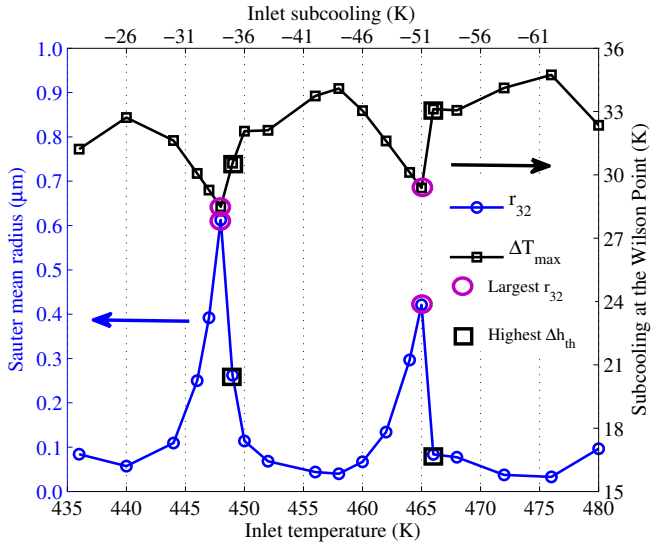

(b) Sauter mean radius and Wilson point subcooling

Figure 1. Wilson point conditions and downstream droplet size

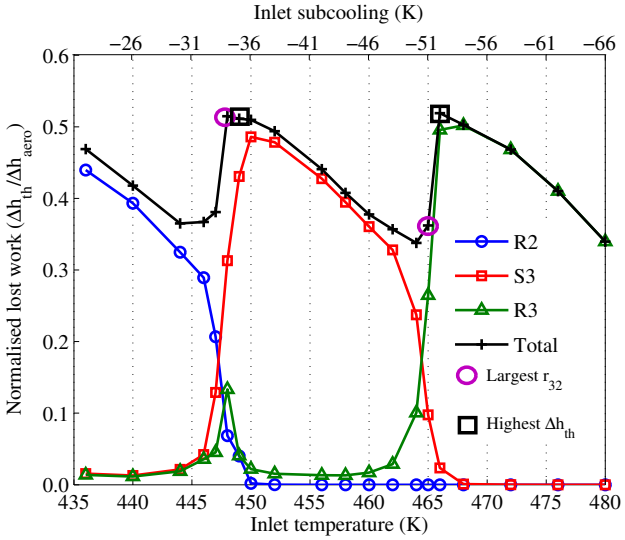

(a) Thermodynamic losses

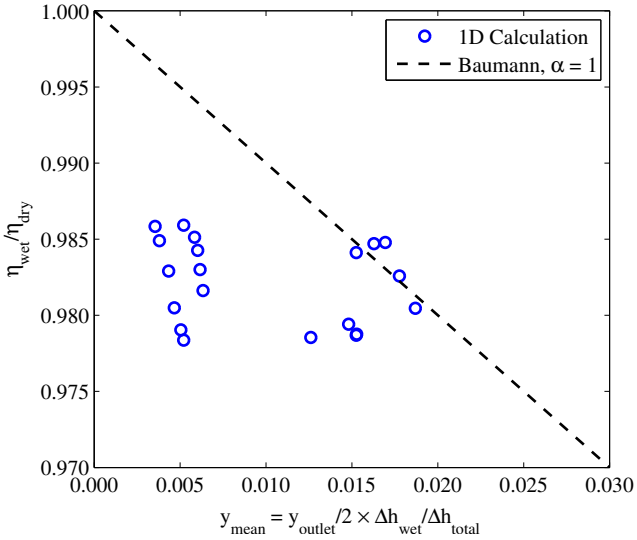

(b) Wet vs. dry efficiency

Figure 2. Variation of lost work due to phase change and a comparison with Baumann loss

drops significantly when the Wilson point occurs at the very end of the high expansion rate region, as nucleation is quenched by the sudden reduction in expansion rate. Any further increase in inlet temperature will move the Wilson point into the following blade row. The low peak subcooling causes fewer droplets to be nucleated, resulting in a large downstream droplet size. The inlet temperatures that correspond to the largest downstream droplets as well as the highest levels of phase change loss Δh_{th} (see Eq. 8 below) are labelled in Fig. 1b. The cases with the highest loss do not correspond to those with the largest droplets.

The thermodynamic loss generated in each of the last three blades is plotted against inlet temperature and inlet subcooling in Fig. 2a. The loss due to phase change Δh_{th} is normalised using the total viscous loss specified Δh_{aero}. The specified viscous loss causes a 4% efficiency reduction. The total phase change loss therefore varies between 1.6% and 2.0% of the total enthalpy drop. The loss curves for each individual row have the same shape and are offset by the blade row static temperature drop which is about 18 K.

The most work is lost due to irreversible phase change when T_{in} = 449 K and 466 K. At these temperatures the Wilson point is located as early as possible in the given blade row, at the beginning of the high expansion rate region. The Wilson points are in S3 and R3, respectively, and the flow has a high level of subcooling throughout the region of low expansion rate that extends backwards to the previous blade row. While the nucleation in this region is not sufficient to return the flow to equilibrium, some droplets are formed and the associated irreversible heat transfer causes the high level of loss. These cases do not correspond to the maximum Wilson point subcooling values seen in Fig. 1b (T_{in} = 440 K, 458 K, and 476 K), but rather have the largest high-subcooling zone. This indicates that the whole subcooling history of fluid particles determines the total thermodynamic loss, not the extreme values of subcooling.

Conversely, low thermodynamic loss occurs when the Wilson point is at the very end of a high expansion rate zone. In these cases nucleation is quenched by the reduction in expansion rate, resulting in lower values of peak subcooling and peak nucleation rate than would otherwise occur. This is also the cause of the spikes in Sauter mean radius seen in Figure 1b when T_{in} = 448 K and 465 K. The large droplet sizes correspond to low values of thermodynamic loss in the nucleation zone. However, these cases will see increased loss in the downstream stages if the relatively few droplets cannot grow quickly enough to maintain near-equilibrium flow conditions at high expansion rates. This effect is seen when T_{in} = 448 K. The nucleation loss in R2 is low but the resulting droplets are so large that some secondary nucleation occurs in R3 causing further entropy generation (see Fig. 2a).

Fig. 2b plots the ratio of two-phase efficiency η_{wet} to dry efficiency η_{dry} against the mean wetness fraction y_{mean} which is defined in the figure. The calculated values can be compared to the stage efficiencies predicted by the Baumann rule in the form used by Kreitmeier et al.[28],

$$\eta_{wet} = \eta_{dry}(1 - \alpha y_{mean}). \tag{6}$$

α is the Baumann factor and is typically taken to equal 1. The mean wetness fractions shown here are lower than those typically presented[29] because there is at most one stage downstream of nucleation. Only the thermodynamic loss is included in the calculation. Within the nucleating stage ($y_{mean} < 1\%$) the thermodynamic loss is significantly more than what the Baumann rule indicates. The phase change loss is dominated by **wetness formation in the nucleating stage** and is not appreciably increased by the **further** droplet growth in the stage following nucleation. The Baumann estimate is therefore more accurate when at least two wet stages are considered. The location of the Wilson point within the repeating expansion profile changes the wet efficiency by as much as 0.8% for very similar mean wetness levels.

Repeating Stage Design

The impact of wake-chopping is now investigated using a three-stage Q3D geometry. The blade geometry is representative of the first three stages of the five stage ALSTOM test turbine described by Kreitmeier et al.[28] The centre-line radius is held constant while the streamtube thickness is increased to maintain consistent Mach numbers and flow angles through the three stages.

The repeating stage condition has several advantages for the investigation of wake-chopping. It prevents confounding issues of differing expansion profiles (both pitchwise and axially) in adjacent blades, which may alter the characteristics of the Wilson zone when it is moved between them. Furthermore, the dissipation of the upstream wake will occur similarly in each blade.

Although the geometry is based on a test-scale turbine, the repeating stage was scaled to full size (rotational speed 3000 RPM) for this analysis. The centreline radius for the full-scale case is 1.0 m, which places the Q3D test section at approximately mid-span in the third stage. The flow is axial at inlet, and the pressure ratio (PR) within each blade is determined by the amount of turning needed to return the relative flow angle to 0° at the entrance to the next blade. For the selected geometry, this results in a single blade pressure ratio of 1.30. The amount of radial expansion required by the streamtube to maintain the velocity triangles and Mach numbers while accommodating the reduction in fluid density can be estimated using a polytropic relationship:

$$\frac{V_2}{V_1} = \left(\frac{P_1}{P_2}\right)^{\frac{1}{\gamma\eta}}. \tag{7}$$

With the given pressure ratio, an isentropic exponent of 1.32 for steam, and an assumed polytropic efficiency of 0.9, the required volume ratio per blade is 1.25. The streamtube expansion occurs within the blade and the radial height is kept constant in the inter-row gaps. The blade spacing is approximately 60% of the axial chord and is constant between all blade rows.

The mesh is generated using NUMECA Autogrid5. To ensure a grid-independent solution, the three stage case was calculated using a series of increasingly fine grids, details of which are shown in the upper portion of Tab. 1. The mass flow rate, total-to-static isentropic efficiency for three stages, and outlet wetness fraction are also included. Each calculation is converged to less than 0.01% average error in ρv_x and less than 0.1% error in mass flow.

Grid Comparison	**Coarse**	**Medium**	**Fine**
Total grid points	519,240	1,145,940	2,017,440
Mass flow ratio, $\dot{m}/\dot{m}_{fine}$	1.014	1.005	1.000
Isentropic efficiency, $\eta_{tt} - \eta_{tt,fine}$	1.8%	0.3%	0.0%
Outlet wetness fraction, y_{out}	2.74%	2.72%	2.70%
Mean Flow Conditions		**Medium**	
Blade PR		1.30	
$Ma_{rel,out}$		0.675	
β_{out}		71.2°	
Φ		0.35	
Ψ		0.96	

Table 1. Grid points and selected results for three mesh densities

The lower portion of Tab. 1 presents the mean flow parameters calculated for all three stages using the medium-density mesh. The maximum variation from the mean blade pressure ratio is less than 5%. The outlet relative Mach number shown is the mean of the pitchwise average values recorded 25% of an axial chord downstream of each trailing edge. Again, the values at individual trailing edges vary by less than 5% from this mean. The relative exit angle, the flow coefficient Φ, and stage loading coefficient Ψ are also included in Tab. 1. The flow coefficient and stage loading coefficient decrease through the stages due to the reduction in velocities needed to maintain consistent Mach numbers as the flow expands. Therefore the mean quantities shown here are lower than typical design values.

For the unsteady simulations, the blade passing period is divided into 100 time-steps, 25 of which are saved for subsequent analysis. 150 explicit "internal" iterations are performed at each "external" time-step; this relatively high number is needed to ensure a periodic wetness solution. 25 blade passing cycles were simulated to achieve periodic variations in both pressure and wetness fraction.

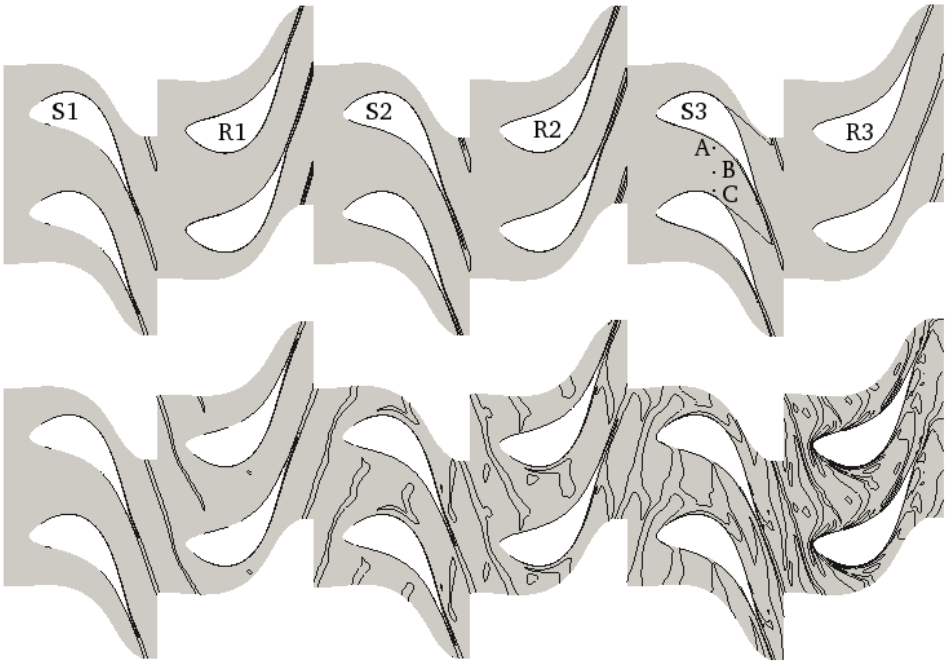

Figure 3. Steady (top) and unsteady (bottom) mixture entropy contours

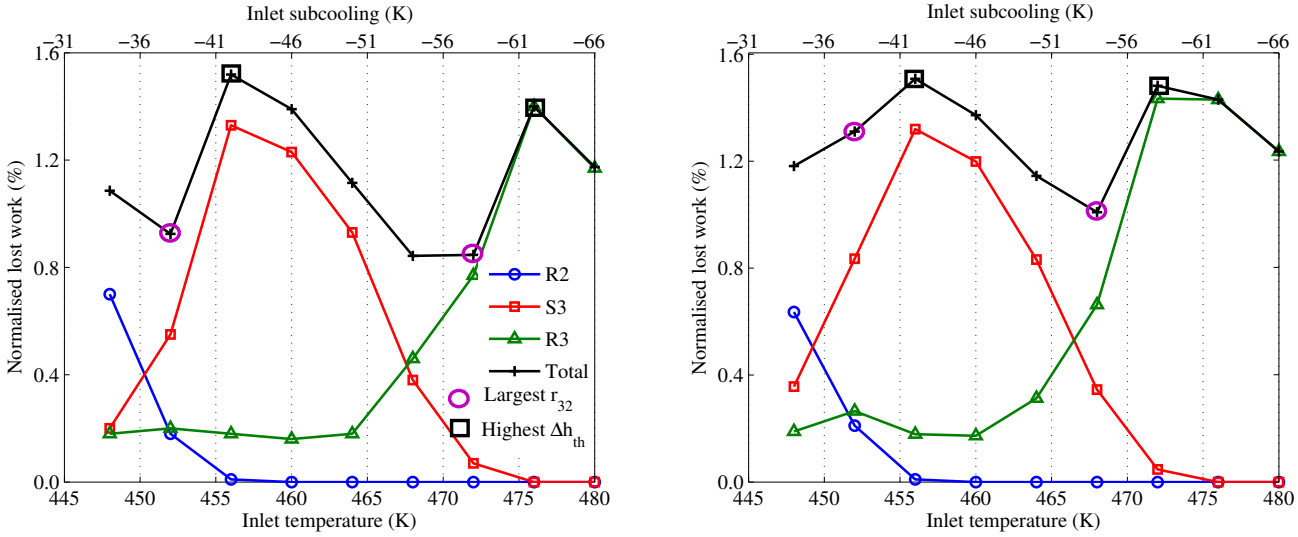

(a) Steady **(b)** Unsteady

Figure 4. Variation of lost work due to phase change with inlet temperature

Repeating Stage Results

The Q3D geometry described above has been simulated in STEAMBLOCK under both steady and unsteady conditions. In the steady case, a mixing plane is used to average the flow conditions between each blade row, while in the unsteady case values are transferred between the blade rows via a slip-plane. Fig. 3 shows mixture entropy contours for both a steady (top) and unsteady (bottom) case with inlet temperature equal to 464 K. The averaging caused by the mixing plane between each blade row is clearly visible in the steady result, while in the unsteady case the wakes can be observed to persist through multiple downstream blade rows. The nucleation zone can be identified in the steady case where an entropy contour crosses the passage near the trailing edge of S3.

In this case, the number of blades in each row is constant and the relative circumferential (or “clocking”) position of the stators is such that wakes from one row will travel through the passage centre of the following row. The impact of varying blade numbers and changing the relative clocking positions on these unsteady effects requires further study.

Steady and unsteady calculations have been performed for inlet temperatures between 448 K and 480 K, with increments of 4 K. The inlet subcooling varies from -34 K to -66 K. In the coldest cases nucleation begins in R2 and in the hottest cases it is delayed until R3. The work lost due to non-equilibrium effects within each blade row

for both steady and unsteady cases is plotted against inlet temperature (bottom) and inlet subcooling (top axis) in Fig. 4. The values of thermodynamic loss have been normalised using the unsteady work output at each temperature. The bulk of the entropy due to irreversible phase change is generated **by droplet growth within** the nucleating blade. The loss curves for S3 and R3 are remarkably similar and are offset by the blade temperature drop which is just over 20 K. The R2 curve is not complete but appears to be following the same trajectory. This indicates that wetness formation is occurring similarly within each row. The cases that produce the highest phase change loss and the largest Sauter mean radius are marked in Fig. 4.

These plots contain the same features as the loss curve from the single streamline investigation, Fig. 2a. In the steady case, two distinct maxima are visible at T_{in} = 456 K and T_{in} = 476 K. The inlet temperatures with the minimum loss are just below those with the maximum loss. The trends are similar although less dramatic in the unsteady cases. The T_{in} = 456 K case also has high loss in the unsteady simulation, but the T_{in} = 476 K case is eclipsed by T_{in} = 472 K, which had nearly the lowest loss in the steady simulation.

Figure 5 allows a comparison of the calculated efficiency reduction due to irreversible phase change and the Baumann rule. As with the 1D case, the mean wetness fractions are low because at most one stage downstream of nucleation is modelled. There is significant scatter in the steady results, with over 1% change in efficiency between simulations with 0.4% and 0.5% mean wetness. The scatter is reduced in the unsteady cases where the range in efficiencies is 0.5%. In the steady simulations, the Wilson zone location is a strong driver of thermodynamic loss. This is also true in the unsteady simulations, but the effect is diluted because the Wilson zone location oscillates as wake flow is swept through the passage. A Baumann factor of $\alpha = 1$ underestimates the loss within the nucleating stage, but is more satisfactory for multiple wet stages (i.e. $y_{mean} > 1\%$). The Baumann loss appears to be an overestimate when $y_{mean} > 1.5\%$, but in this region other wetness loss mechanisms not considered here will also be present.

The Sauter mean radii predicted at the outlet of the steady and unsteady cases are shown in Fig. 6. Two peaks are seen in the steady result at T_{in} = 452 K and T_{in} = 472 K, while in the unsteady calculation the maximum droplet size occurs at T_{in} = 452 K and T_{in} = 468 K. **These correspond to the temperatures at which the minimum entropy is generated from irreversible phase change. This is because the majority of the irreversible heat transfer occurs during the intense droplet growth immediately after nucleation. In these cases nucleation occurs very near to the trailing edge and is artificially quenched by the following mixing plane. This reduces the subcooling, lowering the rate of droplet growth and irreversible heat transfer. The fewer droplets nucleated grow to large size in the next blade row in order to achieve the equilibrium wetness fraction.** This was also seen in the 1D calculation above (Fig. 1b).

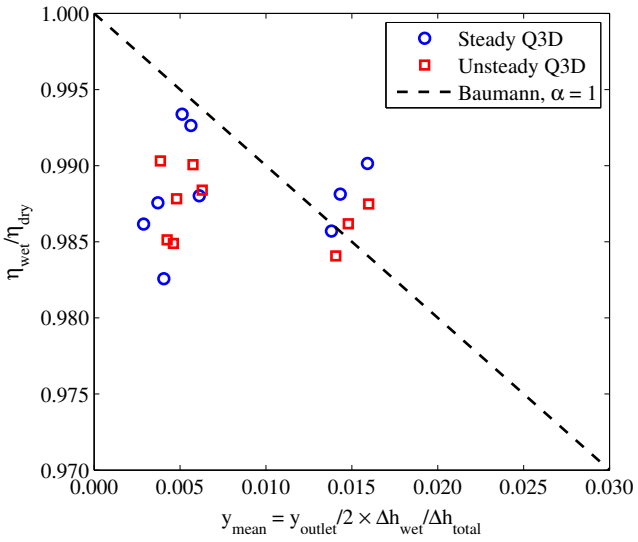

Figure 5. Wet vs. dry efficiency and the Baumann loss prediction

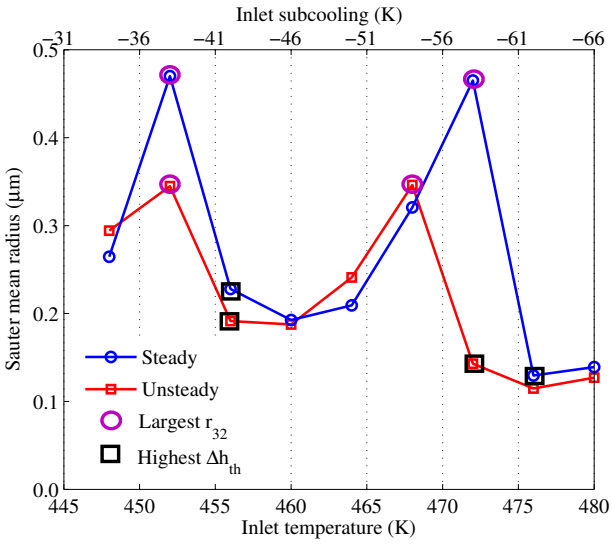

Figure 6. Variation of Sauter mean radius with inlet temperature

Nucleation in the Unsteady Flow Field

Figure 7 plots the gas temperature and nucleation rate at three locations in S3. The locations are approximately at mid-chord and are indicated in the steady portion of Fig. 3. All three locations are dry but subcooled, and significant nucleation is occuring at point C. In the steady result, the pressure side temperature at point A is 358 K (ΔT = 17.0 K), the passage centre temperature at point B is 355 K (ΔT = 19.5 K), and the suction side at point C has already cooled to 341 K (ΔT = 28.8 K). The presence of high- and low-entropy regions in the unsteady calculation causes the local gas temperature to vary by about 5 K, as shown in Fig. 7a. Due to the highly non-linear dependence of nucleation rate on temperature, these small changes have a significant impact on droplet formation. On the suction side at point C, the steady simulation predicts a nucleation rate of 6.7×10^{18}. The unsteady nucleation rate varies between 5.7×10^{16} and 4.1×10^{19}. The time-average of the unsteady nucleation rate is 6.2×10^{18}, notably similar to the steady

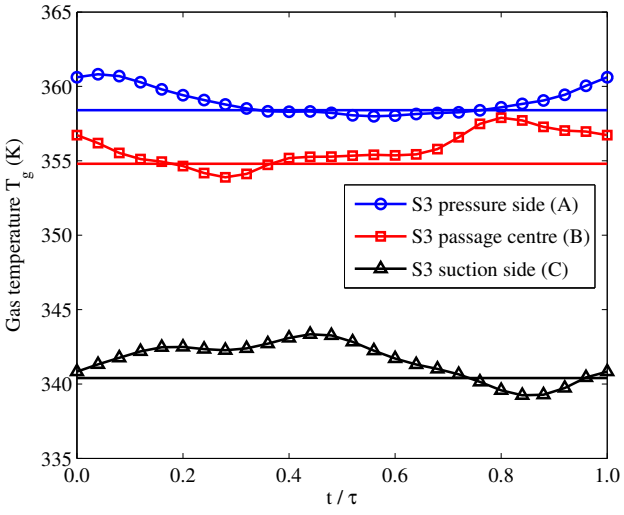

(a) Temperature

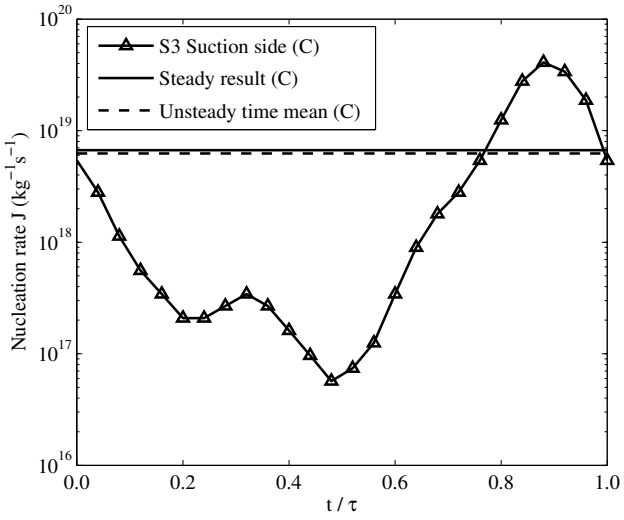

(b) Nucleation rate

Figure 7. Temperature and nucleation rate at three points in S3

prediction. However, the unsteady variations in nucleation rate will affect the droplet spectrum (see Fig. 9 below).

Steady and unsteady subcooling contours are shown for four inlet temperatures in Fig. 8. Steady contours are shown in the top half of each figure. Examining the variations in subcooling gives insight into droplet nucleation and growth (Eqs. 2 and 4) as well as the resulting thermodynamic loss. This is calculated by summing the lost work due to irreversible phase change within every grid cell[24]:

$$\Delta h_{th} = \sum_{i=1}^{n} T_{exit} \frac{\Delta T}{T_g T_s} h_{fg} \cdot [4\pi \rho_f G \mu_2] \cdot \rho \cdot VOL, \quad (8)$$

where G is the local droplet growth rate calculated via Eq. 4, ρ is the mixture density, and VOL is the volume of the local grid cell. The term in brackets gives the increase in wetness fraction within the current cell. **Eq. 8 assumes the droplet temperature is equal to the local saturation temperature, i.e. the effect of capillarity is neglected. This causes the loss generated by small droplets to be overestimated but should not affect the results presented here.**

Subcooling contours are shown at $\Delta T = 20$ K (white) and at integer values between 28 K and 32 K (black). The nucleation zone can be identified where the higher subcooling contours are clustered together. Subcooling above $\Delta T = 20$ K causes nucleation at a level too low to reach the Wilson point. Nevertheless, droplets are formed and the resulting irreversible heat and mass transfer contributes to the thermodynamic loss. In the case shown in Fig. 8a, $T_{in} = 456$ K and the Wilson zone occurs early in S3. The Wilson zone is preceded by a large region of high subcooling $\Delta T \geq 20$ K stretching back into R2. This large region is present in the steady and unsteady cases, which both have a high thermodynamic loss in Fig. 4. Because the Wilson zone is early in the blade row, any delay caused by wake-chopping will push the Wilson zone into a region of higher expansion rate. Therefore the loss and Sauter mean radius are not sensitive to wake-chopping.

Figures 8b and 8c show cases with $T_{in} = 464$ K and 468 K, respectively. The higher inlet temperature is shifting the Wilson zone progressively further downstream in S3 and reducing the size of the $\Delta T \geq 20$ K region. The thermodynamic loss is therefore reduced. When $T_{in} = 464$ K, the Wilson zone is entirely contained within S3 and no fluid remains highly subcooled into R3. When $T_{in} = 468$ K, however, some fluid particles reach the S3-R3 boundary with $\Delta T \geq 20$ K. In the steady case, the averaging performed by the mixing plane artificially reduces the level of subcooling and no further nucleation occurs. In the unsteady case, some further nucleation occurs in these fluid particles in R3. This case is more sensitive to wake-chopping because the presence of high-entropy flow causes nucleation to be delayed past the high expansion region to the inter-row gap and the following blade.

The case in which $T_{in} = 472$ K is the most sensitive to wake-chopping. As when $T_{in} = 468$ K, nucleation in the steady case is quenched by the reduction in expansion rate after the trailing edge, and the high subcooling is artificially eliminated by the mixing plane. Although subcooling of $\Delta T \geq 20$ K occurs in R3, this causes only droplet growth and no further nucleation occurs. This case has a low thermodynamic loss and a very large Sauter mean radius. Because this averaging does not occur in the unsteady case, there is substantial further nucleation within R3. The further nucleation reduces the Sauter mean radius while the larger region of high subcooling increases the thermodynamic loss.

Figure 9 presents the steady and unsteady droplet spectra at the outlet for the same four inlet temperatures. The spectra are created by compiling the liquid mass flow rate and Sauter mean radius at every circumferential grid point at the outlet, as well as every time frame in the unsteady case. Multiple droplet radii in a steady case indicate a variation in Sauter mean radius across the passage.

Unsteady effects do not significantly modify the droplet spectrum for the first case, $T_{in} = 456$ K, although the unsteady spectrum contains droplets both larger and smaller than the steady spectrum. The Wilson zone in both cases is contained within the high expansion region of S3 and produces many droplets that do not grow to large size. The Wilson zone becomes increasingly sensitive to wake-chopping as the inlet temperature rises and it is moved

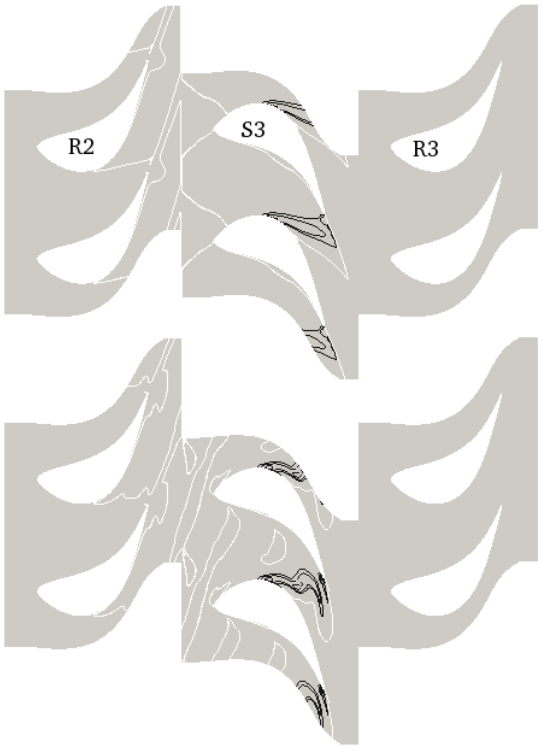

(a) T_{in} = 456 K

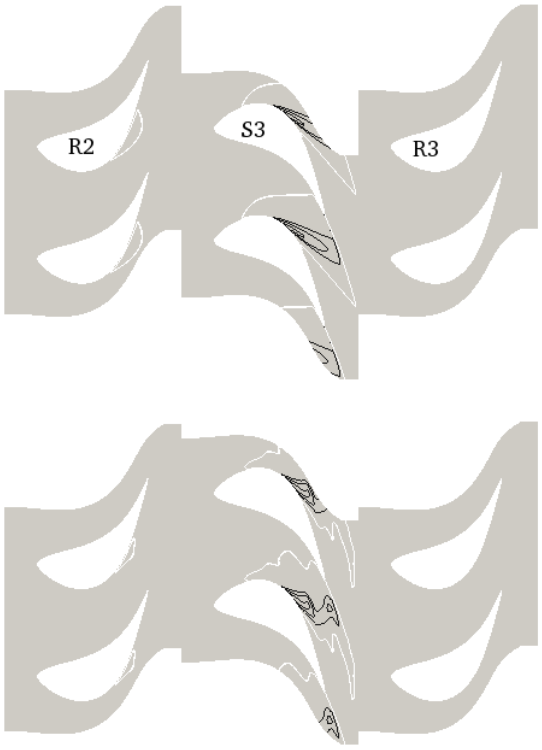

(b) T_{in} = 464 K

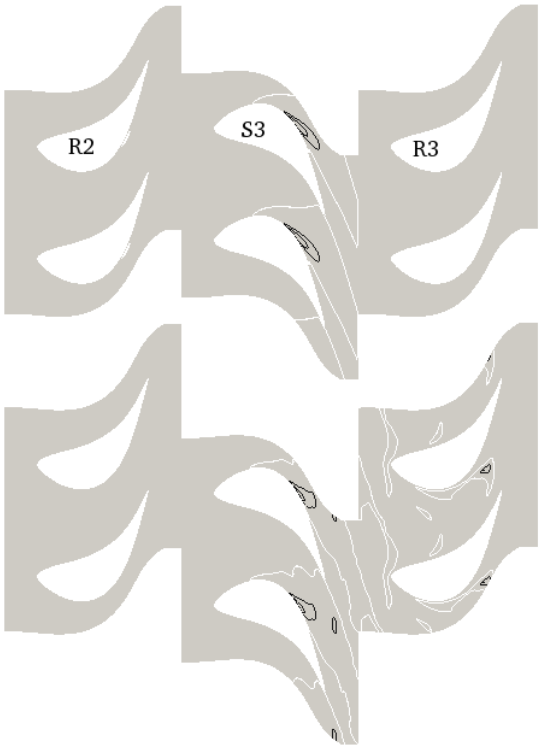

(c) T_{in} = 468 K

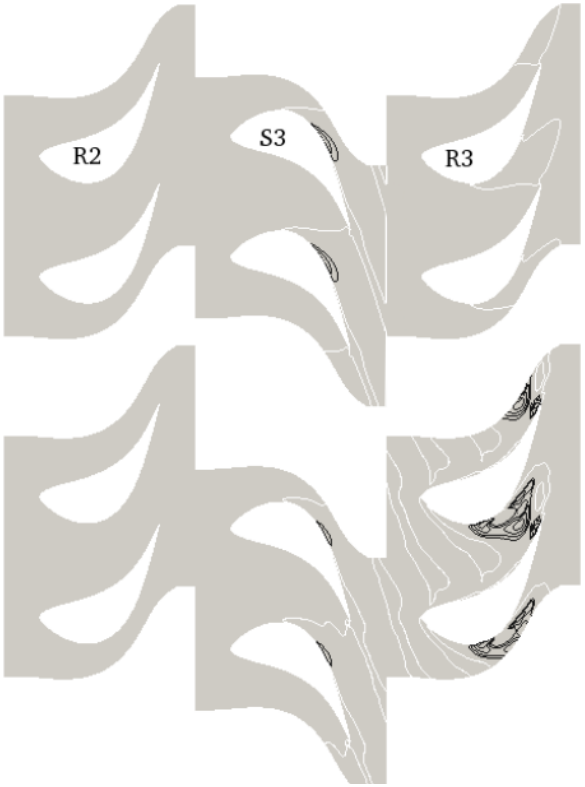

(d) T_{in} = 472 K

Figure 8. Subcooling contours for four inlet temperatures. Contours shown at ΔT = 20 K (white), 28 K, 29 K, 30 K, 31 K, and 32 K.

towards the S3 trailing edge and inter-row gap. This is reflected in the broadening of the unsteady droplet spectra.

When $T_{in} = 468$ K and 472 K, the steady Wilson zone occurs just upstream of the trailing edge. The end of the high expansion rate region quenches the spontaneous condensation, and the remaining subcooling is reduced when the mixing plane averages across both wet and dry flow. The existing droplets grow to large size during the expansion through R3. In the unsteady cases, nucleation is divided between S3 and R3. The coldest freestream fluid nucleates near the S3 trailing edge; these droplets grow substantially within the inter-row gap and form the "tail" of droplets that

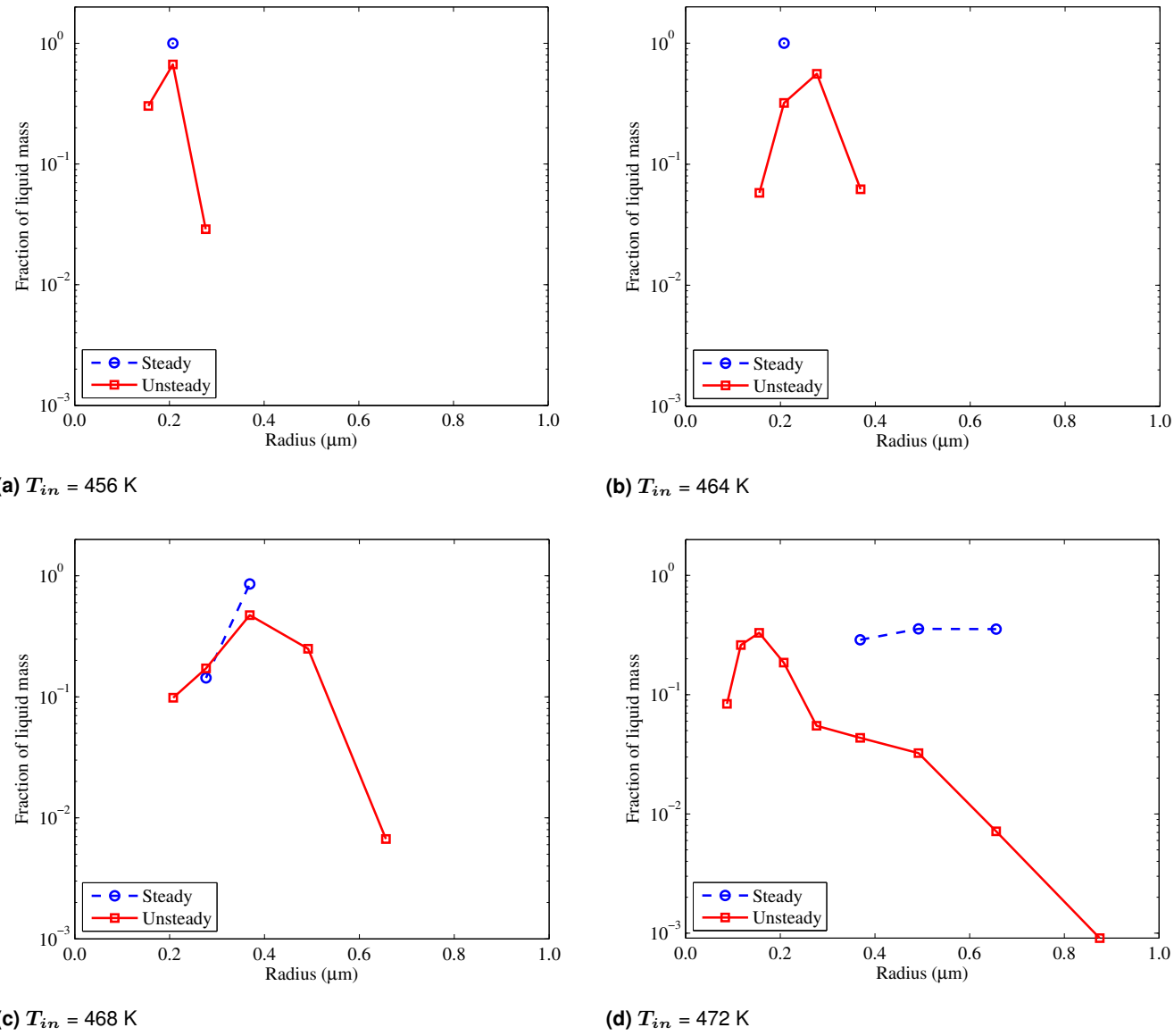

(a) T_{in} = 456 K

(b) T_{in} = 464 K

(c) T_{in} = 468 K

(d) T_{in} = 472 K

Figure 9. Droplet spectra for four inlet temperatures

extends past $r = 0.5$ μm. Nucleation in the warmer wake fluid is delayed completely into R3, where the smaller droplets in the spectrum ($r \leq 0.3$ μm) are produced. Although very large droplets are present in the unsteady spectrum, the many small droplets mean that the overall Sauter mean radius is still low ($r_{32} = 0.15$ μm for $T_{in} = 472$ K).

Conclusion

The calculations presented here provide insight into the relation between the Wilson zone location within a blade row and the resulting entropy generation and droplet spectrum. The phase change loss will be highest when a large region of high subcooling is present because more irreversible heat transfer occurs within this extended high-subcooling zone. This case is not generally that which has the highest peak subcooling value. The lowest phase change loss is generated when the Wilson zone occurs at the very end of a blade row or within the inter-row gap. The loss reduction between the highest ($T_{in} = 456$ K) and lowest ($T_{in} = 468$ K) loss cases in the unsteady Q3D simulations was equivalent to 0.5% of the work output for the three stages. However, in the cases with low loss in the Wilson zone, large droplets are produced which may cause more irreversible heat transfer in the downstream blade rows. The loss in the nucleation region must be balanced against the downstream irreversible heat transfer and other wetness loss mechanisms which increase with droplet size[29]. The thermodynamic loss in the nucleating stages is driven by the expansion rate variation in and around the Wilson zone rather than mean wetness fraction as assumed in the Baumann rule.

These results indicate that wake-chopping contributes to the characteristic shape of the experimental droplet spectra measured by Young et al.[30] in operating steam turbines. Young et al. observed turbine spectra which contained a peak at relatively low radius followed by a long tail of droplets reaching radii over 0.5 μm, spectra similar to that of Fig. 9d. Steady calculations do not predict this type of droplet spectrum and in the present case can underpredict the level of thermodynamic loss in the nucleating stage by

up to 40%. The current findings are also consistent with the measurements reported by Chandler et al.[31] in a five stage model turbine. Chandler et al. measured the overall turbine efficiency and the attenuation of two frequencies of light within the two-phase flow prior to the last turbine stage. The variations in light attenuation and efficiency match the trends seen in the present work.

Although only a specific case has been analysed, the effects shown are common to all condensing flows in turbines. Understanding the relation between steam turbine pressure profiles, wake-chopping, thermodynamic wetness loss, and the resulting droplet spectra is necessary to make design changes to minimise total wetness loss. The present findings demonstrate that thermodynamic loss in both the nucleating stage and the downstream stages can be reduced if the Wilson zone is contained within the high-expansion-rate region of a single blade row.

Acknowledgements

The first author, FRH, is grateful for the support of a Cambridge International Scholarship provided by the Cambridge Commonwealth, European, and International Trust in collaboration with ALSTOM. All authors wish to acknowledge generous support from ALSTOM Power (Steam Turbines Division).

References

1. Gyarmathy G. *Basis of a theory for wet steam turbine*. Dissertation, ETH Zürich, 1962. Translation into English.
2. Moore MJ, Walters PT, Crane RI et al. Predicting the fog-drop size in wet-steam turbines. In *Heat and Fluid Flow in Steam and Gas Turbine Plant*.
3. Moses CA and Stein GD. On the growth of steam droplets formed in a laval nozzle using both static pressure and light scattering measurements. *Trans ASME, J Fluids Eng* 1978; 100: 311–322.
4. Starzmann J, Hughes FR and White AJ. Results of the international wet steam modelling project. In *Proc. Wet Steam Conference, 12–14 Sep.* Prague, CZ.
5. Wróblewski W, Dykas S and Gepert A. Steam condensing flow modeling in turbine channels. *Int J Multiphase Flow* 2009; 35: 498–506.
6. Simpson DA and White AJ. Viscous and unsteady flow calculations of condensing steam in nozzles. *Int J Heat and Fluid Flow* 2005; 26: 71–79.
7. White AJ, Young JB and Walters PT. Experimental validation of condensing flow theory for a stationary cascade of steam turbine blades. *Phil Trans R Soc A* 1996; 354: 59–88.
8. Chandler KD. *Unsteady Wetness Effects in Low Pressure Steam Turbines*. PhD Thesis, Cambridge University Engineering Department, 2013.
9. Guha A and Young JB. The effect of flow unsteadiness on the homogeneous nucleation of water droplets in steam turbines. *Phil Trans R Soc A* 1994; 349: 445–472.
10. Petr V and Kolovratnik M. Modelling of the droplet size distribution in a low-pressure steam turbine. *Proc IMechE, Part A: J Power and Energy* 2000; 214(A2): 145–152.
11. Denton JD. An improved time marching method for turbomachinery flow calculation. In *ASME 1982 Int. Gas Turb. Conf. and Expo.*
12. Chandler KD, White AJ and Young JB. Unsteady wetness effects in lp steam turbines. In *ASME Conf. Proc. Turbo Expo*.
13. Pullan G and Denton JD. Numerical simulations of vortex-turbine blade interaction. In *Proc. of the 5th E.T.C.*
14. Jameson A. Time dependent calculations using multigrid, with applications to unsteady flows past airfoils and wings. *AIAA Paper* 1991; 1596.
15. Allmaras SR and Johnson FT. Modifications and clarifications for the implementation of the spalart-allmaras turbulence model. In *7th Int. Conf. on CFD (ICCFD7)*. pp. 1–11.
16. Denton JD. The calculation of three dimensional viscous flow through multistage turbomachines. In *ASME 1990 Int. Gas Turb. and Aero. Conf. and Expo.*
17. Jameson A, Schmidt W and Turkel E. Numerical solutions of the euler equations by finite volume methods using runge-kutta time-stepping schemes. *AIAA Paper* 1981; 1259.
18. Hill PG. Condensation of water vapour during supersonic expansion in nozzles. *J Fluid Mech* 1966; 25: 593–620.
19. White AJ and Hounslow MJ. Modelling droplet size distributions in polydispersed wet-steam flows. *Int J Heat and Mass Trans* 2000; 43(11): 1873–1884.
20. Hill PG, Miyagawa K and Denton JD. Fast and accurate inclusion of steam properties in two-and three-dimensional steam turbine flow calculations. *Proc Inst Mech Eng C, J Mech Eng Sci* 2000; 214(7): 903–919.
21. IAPWS. Release on the iapws industrial formulation 1997 for the thermodynamic properties of water and steam, 2007.
22. Bakhtar F, Young JB, White AJ et al. Classical nucleation theory and its application to condensing steam flow calculations. *Proc Inst Mech Eng C, J Mech Eng Sci* 2005; 219(12): 1315–1333.
23. Kantrowitz A. Nucleation in very rapid vapour expansions. *J Chem Phys* 1951; 19(9): 1097–1100.
24. Young JB. The spontaneous condensation of steam in supersonic nozzles. *Physicochemical hydrodynamics* 1982; 3(1): 57–82.
25. Hughes FR, Starzmann J, White AJ et al. A comparison of modeling techniques for polydispersed droplet spectra in steam turbines. *Trans ASME, J Eng Gas Turb Power* 2016; 138(4): 042603.
26. Hughes FR. *Throughflow Methods for Two-Phase Flow in Steam Turbines*. PhD Thesis, Cambridge University Engineering Department, 2016.
27. Young JB. Two-dimensional, nonequilibrium, wet-steam calculations for nozzles and turbine cascades. *Trans ASME, J Turbomach* 1992; 114(3): 569–579.
28. Kreitmeier F, Greim R, Congiu F et al. Experimental and numerical analyses of relaxation processes in LP steam turbines. *Proc Inst Mech Eng C, J Mech Eng Sci* 2005; 219(2): 1411–1436.
29. Starzmann J, Casey M, Mayer JF et al. Wetness loss prediction for a low pressure steam turbine using cfd. *Proc IMechE, Part A: J Power and Energy* 2014; 228(2): 216–231.
30. Young JB, Yau KK and Walters PT. Fog droplet deposition and coarse water formation in low-pressure steam turbines: a combined experimental and theoretical analysis. *Trans ASME, J Turbomach* 1988; 110: 163–172.
31. Chandler KD, Melas M and Jorge T. A study of spontaneous condensation in an lp test turbine. In *ASME Conf. Proc. Turbo Expo*.